In situ temperature profile measurements with high-energy X-rays as a probe of optical floating zone crystal growth environment

Jonathan J. Denney,[a] Yusu Wang,[a] Adam A. Corrao,[a] Guanglong Huang,[b] David Montiel,[b] Hui Zhong,[c] Eric Dooryhee,[d] Katsuyo Thornton[b] and Peter G. Khalifah[a,e]*

[a]Department of Chemistry, Stony Brook University, Stony Brook, NY 11794, USA, [b]Department of Materials Science and Engineering, University of Michigan, Ann Arbor, MI 48109, USA, [c]Joint Photon Sciences Institute, Stony Brook University, Stony Brook, NY 11794, USA, [d]National Synchrotron Light Source II, Brookhaven National Laboratory, Upton, NY 11973, USA, and [e]Department of Chemistry, Brookhaven National Laboratory, Upton, NY 11973, USA. *Correspondence e-mail: kpete@bnl.gov

The ability of optical floating zone (OFZ) furnaces to rapidly produce large single crystals of complex emerging materials has had a transformative effect on many scientific fields that require samples of this type. However, the crystal growth process within the OFZ furnace is not well understood owing to the challenges involved in monitoring the high-temperature crystal growth process. Novel beamline-compatible optical furnaces that approximate the inhomogeneous growth environment within an OFZ furnace have been fabricated and tested in high-energy synchrotron beamlines. It is demonstrated that temperature profiles can be effectively extracted from powder diffraction data collected on polycrystalline ceramic rods heated at their tip. Furthermore, these measured temperature profiles can be accurately reproduced using a heat-transfer model that accounts for solid-state thermal conduction, partial sample lamp power absorption, convective air cooling and radiative cooling, allowing key thermal parameters such as thermal conductivity to be extracted from experimental data.

1. Introduction

Bulk single crystals are of great importance both for industrial applications and for fundamental scientific studies. Within industry, large single crystals play a critical role in a variety of components, including computer chips (Shimura, 2017), lasers (Albers *et al.*, 1986), positron emission tomography detectors for medical imaging (Seidel *et al.*, 1999), infrared night vision scopes (Rogalski & Chrzanowski, 2002) and high-performance turbines for aircraft (Caron & Khan, 1999). Similarly, single crystals are uniquely suited for fundamental studies of the anisotropic intrinsic properties of materials and therefore play a key role in structural studies (Majumdar *et al.*, 2000), inelastic neutron scattering studies of superconductivity and magnetism (Stockert *et al.*, 2008), angle-resolved photoemission studies of electronic states (Damascelli *et al.*, 2003), surface science studies of catalysts (Rodriguez *et al.*, 2007), and studies of the elastic and mechanical properties of solids (Chu *et al.*, 1999). Given the importance of single-crystal samples, methods that can reduce the time needed to develop procedures for single-crystal growth will have a large impact.

In the last quarter-century, the utilization of optical floating zone (OFZ) furnaces for crystal growth has rapidly increased in popularity (Koohpayeh *et al.*, 2008). A common feature of
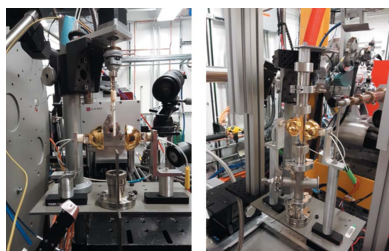
OFZ furnaces is the use of one or more high-power lamps to sustain a narrow melt region (<1 cm in height) between two solid sample rods that are about 5 mm in diameter. The feed rod slowly inserts material into the melt while re-solidification and crystallization of the melt occur on the seed rod as it is pulled down away from the melt, resulting in the growth of crystals as schematically illustrated in Fig. 1. This crystal growth is carried out in a crucible-free manner that can be used to produce crystals with exceptionally low impurity contents, which have been essential for the observation of phenomena such as the *p*-wave superconductivity of Sr_2RuO_4 (Mao *et al.*, 2000). Furthermore, the crystal growth process is relatively fast, with crystals that are 1–10 cm in length being obtained in as little as a day for many systems like $La_2Ti_2O_7$ that melt congruently (Wang *et al.*, 2018), or on a timescale of 1–2 weeks for more challenging incongruently melting systems like many high-T_c cuprate superconductors (Nishimura *et al.*, 1999; Revcolevschi *et al.*, 1999).

Despite the utility of the OFZ crystal growth method in producing high-quality single crystals of complex materials, the OFZ crystal growth process remains relatively poorly understood. This is mainly due to the challenges in obtaining experimental information about the inhomogeneous growth environment within the furnace. The expectation during OFZ crystal growth is that the temperature gradient in the vertical direction is steep (allowing solid and liquid phases to coexist) while the gradient in the horizontal direction (that governs the

Figure 1
Schematic illustration of the OFZ crystal growth process, in which powder from the upper feed rod is lowered into the molten zone at the focal point of the furnace lamp(s) while the lower seed rod is simultaneously pulled down out of the molten zone, promoting crystallization and eventually (through the crystal selection process) resulting in the growth boule terminating in a single crystal.

shape of the solid–liquid interface) is small. These temperature gradients affect numerous aspects of crystal growth, including the height of the molten zone, the shape of the solid–liquid interface (and thus also the crystal selection process), any pre-melting that may occur above the molten zone (and the changes in mass transport that accompany this partial melting), and stoichiometry changes (*e.g.* oxygen loss or cation evaporation) or phase transitions (that may damage the crystal) that may occur in the crystal boule on cooling.

A critical barrier to understanding crystal growth is the difficulty in obtaining quantitative information about temperature gradients present during this process. Direct temperature measurements are hindered by the enclosed nature of the sample environment, while the common indirect measurement technique of pyrometry is hindered by the intense black-body radiation emitted by the heating lamps. In general, temperature information during the growth is completely lacking – OFZ furnaces initiate melting by ramping up the lamp power (without knowledge of the actual temperature), and the growth process is typically only monitored visually on the basis of the images provided using an integrated video camera.

One early effort to modify the crystal growth process to probe temperature gradients involved drilling a hole in the sample seed rod and inserting a thermocouple (Koohpayeh *et al.*, 2009). However, this approach is very laborious, provides no information about horizontal gradients and will run into problems if rods are heated to their melting point. A second effort involved the modification of one OFZ furnace design to enable pyrometry by temporarily closing lamp shutters for a brief (∼60 ms) time (Behr *et al.*, 2010). This method also suffers from limitations – it only records surface temperatures and even though the power interruption is brief, it can adversely affect the crystal growth process.

In order to overcome these limitations, we have explored the use of high-energy X-ray powder diffraction to probe temperature gradients within polycrystalline rods heated with focused lamps at their tip. The high-energy X-rays can penetrate through the ∼5 mm diameter polycrystalline ceramic rods, and the resulting powder diffraction patterns can be analyzed to obtain temperature data when the ceramic thermal expansion properties are known. By scanning the heated sample rod through the beam, it is possible to probe both vertical and horizontal temperature gradients. In this work, we describe the design of novel sample environments that make these experiments possible as well as the measurement and modeling of temperature profiles in heated rods of reference materials.

2. Experimental

Two new sample environments were constructed for experiments, with further details provided in the supporting information. The Mark I furnace consisted of two 150 W halogen reflector lamps (OSRAM 64635 HLX) mounted on stands and a mounting pole with an inverted goniometer head holding an alumina fitting to which a polycrystalline ceramic rod was
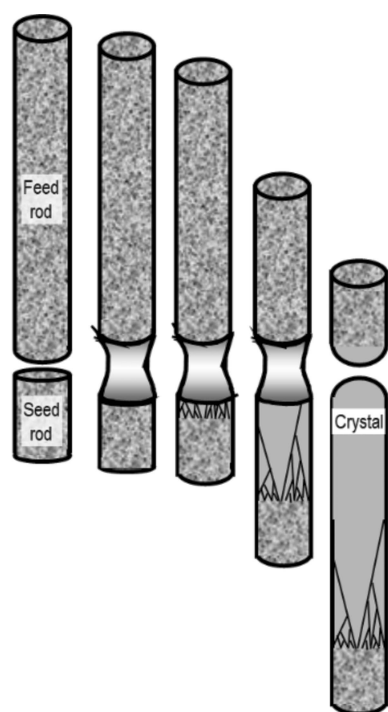
attached with wound wire, allowing the sample to be vertically suspended with the two focal points of light (∼3 mm spot diameter) aimed near the tip of the rod. The Mark II furnace had the lamps mounted in a similar manner but additionally allowed the sample rod to be enclosed within a fused silica tube (25.4 mm outer diameter, 1.5 mm thick) with ports to enable both the evacuation of the tube (to a pressure of ∼100 mTorr = 133 mPa) and the subsequent back-filling with a process gas. The gas inlet line included a pressure-relief check valve to avoid dangerous over-pressurization of the sample chamber. In both cases, the position of the rod was rigidly fixed relative to the lamps – neither rotation nor translation was possible. However, the entire furnace environment was compact enough to readily be translated to allow different portions of the sample to be interrogated with a synchrotron beam.

Polycrystalline ceramic rods were prepared from powders of TiO_2, Al_2O_3 or CuO. For CuO, the particle size was reduced by processing for 5 h in a vibratory mill (Fritsch Pulverisette 0) then for 1 h in a high-energy shaker mill (SPEX 8000). Powders were formed into a rod by loading into a latex balloon (∼6 mm in diameter) and compressing in a hydrostatic vessel with a chamber diameter of 1″ with a force of ∼1.5 × 10⁴ lb (6.8 Mg), corresponding to a hydrostatic pressure of about 2 × 10⁴ psi (138 MPa). After careful removal of the balloon, the pressed rods were heated to increase their density. After sintering at 1100°C for 12 h in air, the TiO_2 rod was 4.78 mm in diameter and 66.5 mm long with a density of 3.70 g cm⁻³ (87% of theoretical) calculated geometrically. After sintering at 1400°C for 24 h in air, the Al_2O_3 rod was 5.01 mm in diameter and 58.9 mm long with a density of 2.19 g cm⁻³ (55% of theoretical). After sintering at 950°C for 24 h under flowing O_2, the CuO rod was 5.73 mm in diameter and 69.2 mm long with a density of 5.86 g cm⁻³ (90% of theoretical).

X-ray diffraction data were collected at the National Synchrotron Light Source II (NSLS-II) at Brookhaven National Laboratory (BNL) on beamline 28-ID-2 (λ = 0.18208 Å) for the Mark I furnace and on 28-ID-1 (λ = 0.1668 Å) for the Mark II furnace. Diffraction data were collected in transmission mode without any collimation beyond the use of slits to select the beam cross section (square, 0.25 × 0.25 mm), resulting in maximum path lengths through the sample of up to ∼6 mm, depending on the rod diameter. Diffraction pattern images were recorded using a PerkinElmer XRD 1621 flat-panel detector with total collection times of 0.2 and 0.1 s and nominal sample-to-detector distances of 1425 and 1000 mm at 28-ID-2 and 28-ID-1, respectively, for diffraction patterns. During synchrotron experiments, data were collected in one of three modalities – constant power line scans on an equilibrated sample (1 mm vertical steps), constant power grid scans on an equilibrated sample (5.57 mm vertical steps and 0.455 mm horizontal steps for TiO_2, and 2.059 mm vertical steps and 0.55 mm horizontal steps for Al_2O_3) or time series (1 s steps) at a single point on the sample measuring the temperature evolution following changes resulting from a jump (up or down) in the lamp power. The

manufacturer-specified motor position reproducibility was 10 μm at 28-ID-2 and 100 μm at 28-ID-1. After equilibrating at a set power level, data collection typically started with a vertical line scan (∼400 s total time) and finished with a grid scan (∼500 s total time), where the former scans were much more severely impacted by the anomalously slow (∼0.1 mm s⁻¹) vertical motor slew rates at beamline 28-ID-2. All vertical and horizontal positions are specified relative to the nominal center of the rod at the height corresponding to the estimated center of the lamp focus, with the coordinate system for the experiment relative to the sample and lamp focus shown in Fig. S1.

The integration and processing of area detector data into 1D diffraction patterns was carried out using the *PyFAI* software package (Ashiotis *et al.*, 2015). Detector calibration was carried out using a self-calibration procedure in which the ceramic phase comprising the rod (*e.g.* TiO_2, CuO) was used to calibrate the sample-to-detector distance and detector tilt using diffraction data collected on the rod prior to heating. For the power jump time series data (for which data were collected at a single spatial location), the detector calibration for integration was carried out once at room temperature for each series. For grid scans and line scans (for which data were collected at multiple spatial locations), the detector calibration for integration was also only carried out at a single spatial location, though a secondary post-processing correction was then also applied to every different spatial position for which diffraction data were collected by separately normalizing the cell volume changes for each point relative to the cell volume determined at room temperature for that specific spatial location. After integration, Pawley refinements (Pawley, 1981) were carried out using *TOPAS* version 6 (Bruker AXS Inc., Madison, Wisconsin, USA; Coelho, 2018) to refine lattice parameters using all reflections with a d spacing greater than $d_{min} = 0.80$ Å (28-ID-2) or $d_{min} = 0.96$ Å (28-ID-1). Refinements were run sequentially in an automated fashion using custom Python scripts written for this purpose. Representative Pawley fits are shown in Fig. S2, and sample refinement control files and data sets are provided as online supporting information.

Temperatures were derived from lattice parameter data using an earlier literature parameterization of the volume expansion of the rutile polymorph of TiO_2, calculated on the basis of synchrotron diffraction experiments carried out using an area detector (Hummer *et al.*, 2007, 2008). These data could be robustly validated against both earlier diffraction experiments and direct dilatometry measurements of thermal expansion. During the analysis, data were corrected so that measurements at room temperature always gave the same calculated temperature of 295 K.

Simulations of thermal profiles within a heated rod of TiO_2 were carried out using the *COMSOL Multiphysics* software (version 5.4; https://www.comsol.com), with the governing equations discussed in more detail in the main text. The sample rod was assumed to have an ideal cylindrical shape with flat ends with a length, diameter and density equal to those experimentally measured for the sample rod.
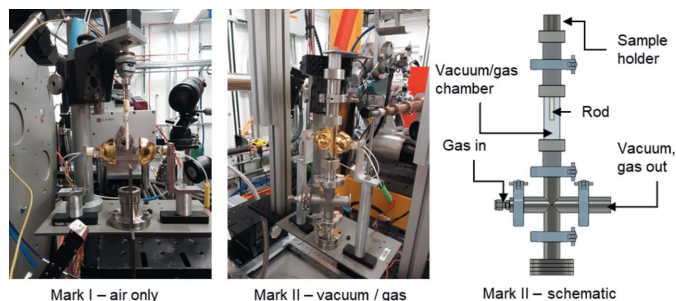
Figure 2
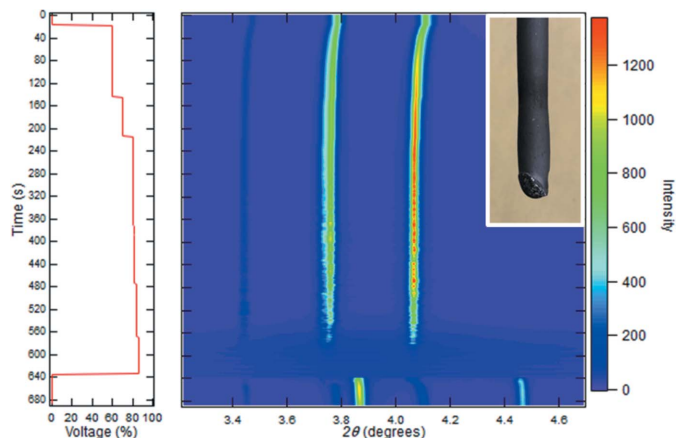Photographs (Mark I and Mark II) and schematic (Mark II) of the mini-FZ furnace.

Figure 3
Waterfall plot of diffraction patterns (right) collected for a CuO rod heated and cooled using the lamp voltage profile shown on the left, with a photograph of the rod at the conclusion of melting shown as an inset. During the experiment, the lamp voltage was turned on to 60%, raised to 80% in 10% steps, raised to 86% in 2% steps, and then turned off.

3. Results and discussion

3.1. Sample environment

As an alternative to pursuing the formidable task of integrating an entire OFZ furnace into a synchrotron beamline, minimalist 'mini-FZ' sample environments were designed to mimic key aspects of the OFZ growth environment at a much smaller scale that could be readily integrated into existing high-energy synchrotron beamlines. Photographs and schematics of the Mark I and Mark II designs of the mini-FZ furnace are shown in Fig. 2. The Mark I design consisted of two main parts: a stand to hold a long polycrystalline rod vertically, and mounts for two 150 W lamps held within integral mirrors that allowed the radiant energy to be focused near the tip of the polycrystalline rod with a focal spot diameter of about 3 mm. The Mark II design was similar in nature, though with the added capability to enclose the sample within a fused silica tube, allowing the sample rod to be heated under a controlled gas or vacuum environment. Further details of the sample environment are provided in the supporting information (Fig. S3).

3.2. Polycrystalline rod melting

In order to be relevant to the study of ceramic melts, the mini-FZ furnace environment should be able to heat the portion of the polycrystalline rod at the focus of the lamps to high temperatures that are well in excess of $1000°C$. Unlike conventional furnaces, the maximum sample temperature will be strongly influenced by the sample physical properties, including the efficiency of light absorption (sample color), the thermal conductance of the rod (which is influenced by both the thermal conductivity of the material and the rod diameter) and the efficiency of cooling (the emissivity of the sample for gray-body radiation and any thermal conduction associated with the process gas environment; Koohpayeh et al., 2009). As such, there is not a well defined maximum temperature that can be ascribed to the mini-FZ furnace.

To demonstrate the capabilities of the mini-FZ furnace, initial tests of ceramic melting were carried out using a poly-crystalline rod ($\sim$5 mm diameter) of CuO whose black color should lead to efficient light absorption over a wide range of visible light energies. These experiments were carried out in an environment of pure O_2 (1 atm = 0.1 MPa) in order to prevent

the reduction of CuO to Cu_2O prior to reaching its melting point of $\sim$1200°C (Kosenko & Emel'chenko, 2001). During heating, the X-ray beam was kept at a single point near the tip of the rod, allowing a time series of diffraction patterns to be collected during heating and cooling. A waterfall plot of the diffraction patterns collected during this experiment (Fig. 3) confirms that no reduction of CuO occurred prior to melting and additionally indicates that melting occurred at a total lamp power of 235 W, which was 78% of the maximum power and 85% of the maximum voltage. On the basis of the previously determined phase diagram for this system, the melt is expected to have a composition of Cu_2O rather than CuO. This is reflected in the diffraction patterns collected after resolidification, which indicated that the rapidly recrystallized solid obtained when the lamps are turned off had more intense diffraction peaks from Cu_2O than from CuO. It has been previously observed that crystal boules of CuO grown in an optical floating zone furnace typically contain undesirable inclusions of Cu_2O (Prabhakaran & Boothroyd, 2003; Ito et al., 1998). The use of in situ diffraction studies to monitor the growth of CuO crystals would aid the identification of growth conditions that prevent the development of these inclusions. Furthermore, the melting points for solvents used for the growth of high-T_c cuprates (Nishimura et al., 1999; Revcolevschi et al., 1999) are very similar to that of CuO, suggesting that growth of this important family of materials can be effectively studied using the infrastructure demonstrated here.

3.3. Steady-state temperature profiles

Although it is generally expected that the temperature gradient during OFZ growth is large in the vertical direction and small in the horizontal direction, the actual magnitude of this gradient is generally unknown. Using the mini-FZ furnace as a proxy for the crystal growth environment, temperature profiles in both the horizontal and vertical direction can be obtained in situ for a heated polycrystalline rod by translating
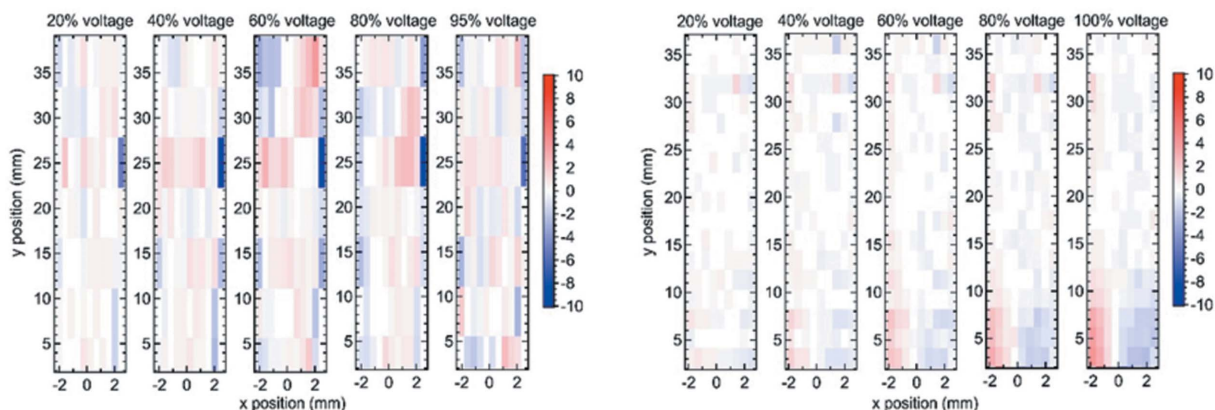
Figure 4
Grid scan results for a TiO$_2$ rod heated in the Mark I furnace (left) and for an Al$_2$O$_3$ rod heated in the Mark II furnace (right). The temperature differences in °C (hotter, red; colder, blue) relative to the average temperature for each height are plotted.

the entire mini-FZ furnace along a line or over a grid so that the high-energy synchrotron beam sequentially probes different regions of the polycrystalline rod. The local temperature at each point can then be determined from the resulting diffraction patterns, taking into account the thermal expansion behavior previously determined for the sample of interest.

The horizontal thermal profiles of a TiO$_2$ rod (measured in the Mark I furnace) and of an Al$_2$O$_3$ rod (measured in the Mark II furnace) obtained from grid scan measurements at different power levels are compared in Fig. 4. The sample position within the furnace was unchanged across all scans. The data have been renormalized so that the temperature difference (relative to the mean temperature for each individual height) is plotted (Fig. 4), with regions having higher than average temperature indicated in red and regions with lower than average temperature indicated in blue. No horizontal gradients due to uneven heating were resolvable within the experimental uncertainty (±2°C, estimated from temperature fluctuations at constant power) for the TiO$_2$ rod heated in the Mark I furnace, while the Al$_2$O$_3$ rod heated in the Mark II furnace had a clear horizontal temperature gradient in which the temperature of the left side of the sample was consistently higher than that of the right side of the sample at all power levels investigated, with a maximum difference of about 6°C near the rod tip. It is expected that this horizontal gradient, when present, is due to imperfect alignment of the two lamps relative to the rod since the same lamps were used in both experiments.

Similar measurement techniques were applied to study the vertical temperature profile of the heated TiO$_2$ rod, with the temperature profile plotted as a function of the lamp power in Fig. 5. It can be seen that the maximum rod temperature increases approximately linearly with the applied voltage (Fig. 5, top), with a maximum temperature of approximately 275°C reached when the lamps were at 95% of the maximum voltage (net lamp power of 282 W). This temperature is far lower than was achieved for CuO, reflecting the lower efficiency of light absorption of white TiO$_2$ (large band gap) than black CuO (medium band gap). As expected, the relative

temperatures decayed more quickly at high temperatures than at low temperatures (Fig. 5, bottom). At each power level, the temperature decayed approximately exponentially with the distance away from the center of the lamp focus (fits shown in Fig. S4), though a more precise description of the temperature profile can be obtained if the thermal properties of the sample
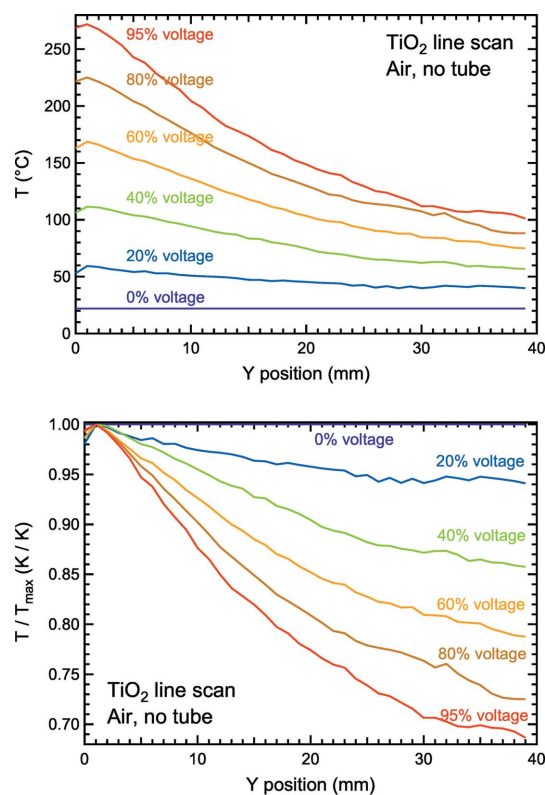

Figure 5
Vertical temperature profiles measured for a TiO$_2$ rod heated at the bottom of its length using the Mark I mini-FZ furnace plotted on an absolute (top) and normalized (bottom) temperature axis. The zero position corresponds to the nominal focus of the lamps used for heating, while positive values correspond to higher vertical positions along the rod. The rods were heated by applying different fractions (0, 20, 40, 60, 80 and 95%) of the maximum voltage for the two 150 W lamps, resulting in actual lamp powers of 25.2, 73.0, 137.2, 215.5 and 282.1 W, respectively.

and its environment are explicitly modeled, as will be done later.

3.4. Dynamic temperature profiles

Additional insights into sample thermal properties can be obtained through the collection of dynamic temperature profiles. In these measurements, the temperature at a single point on the sample rod is followed as a function of time during a power jump time series in which the rod is first heated (lamps turned on to a constant power and held at that power for ~15 min to equilibrate) and then cooled (lamps turned off). Power jump data were collected for three points at the horizontal center of the sample (heights of 0, +10 and +20 mm from the center of the lamp focus) and for three points at the edge of the sample (also at heights of 0, +10 and +20 mm), as shown in Fig. 6 (top). As expected from the line scan data, the temperature decreases as the distance above the lamp focus increases. It was generally found that the temperature at the edge of the rod was slightly higher (3–10°C) than the temperature at the center of the rod. Given that grid scans in which the center and edge temperatures were measured much

closer together in time (<15 s) showed no apparent thermal gradient, it is likely that this center-to-edge difference in power jump data is an experimental artifact, though further testing is needed to confirm this. The time dependence of the temperature rise during power jump experiments was essentially indistinguishable between the edge and center of the rod. When the data sets are renormalized relative to their maximum temperature to facilitate their comparison, it can be seen that the timescale of the temperature rise slows somewhat as the vertical distance from the lamp focus increases (Fig. 6, bottom) during both heating and cooling, reflecting the influence of thermal conduction along the rod. For all positions, the equilibration timescale is approximately 10 min during both heating and cooling, though 90% of the net change typically occurs in the first 3 min.

Upon close inspection (Fig. S5), it can be seen that the diffraction-derived temperature data for TiO_2 have a visible scatter which is on the order of ± 2°C at all times. The magnitude of this scatter is indistinguishable during holds at room temperature (when the lamp is off) and at elevated temperatures (when the lamp is on), suggesting that this scatter is not due to thermal fluctuations. Furthermore, this scatter does not behave in the manner expected for random noise and is instead observed to be roughly periodic with a timescale on the order of 6 s. These fluctuations are therefore believed to be a consequence of small vibrations of the TiO_2 rod as it is suspended from the tall rod on which it is mounted in the Mark I furnace (most likely associated with the lack of stiffness in the goniometer head which was used as the mounting point), though other origins (such as vibrations of the entire motor stack to which the mini-FZ furnace is mounted) cannot be ruled out. Temperature data collected using the Mark II furnace benefit from more rigid sample mounting and do not show significant fluctuations (<0.25°C, Fig. S6), supporting this hypothesis.

3.5. Modeling of temperature profiles

The temperature profile of the heated rods is affected by three main physical processes: (1) the applied heat, determined by the position and efficiency of absorption of radiation from the lamps, (2) the thermal transport of heat within the rod away from the lamp focus, and (3) the heat loss, which occurs either through gray-body radiation (3a) or through thermal conduction of the surrounding atmosphere (3b). These processes are schematically represented in Fig. S7. In the absence of other contributions, the sample temperature can be predicted using a set of four governing equations that quantitatively describe these processes during both steady-state and dynamic heating experiments.

The incoming radiation from the lamps was modeled as a power source applied uniformly over a cylindrical surface strip at the bottom end of a polycrystalline sample rod that was 3 mm in height with a total surface area of $A = 45.05$ mm^2 according to the experimentally measured rod radius. The contribution from the applied heat source at each point in the region is modeled as
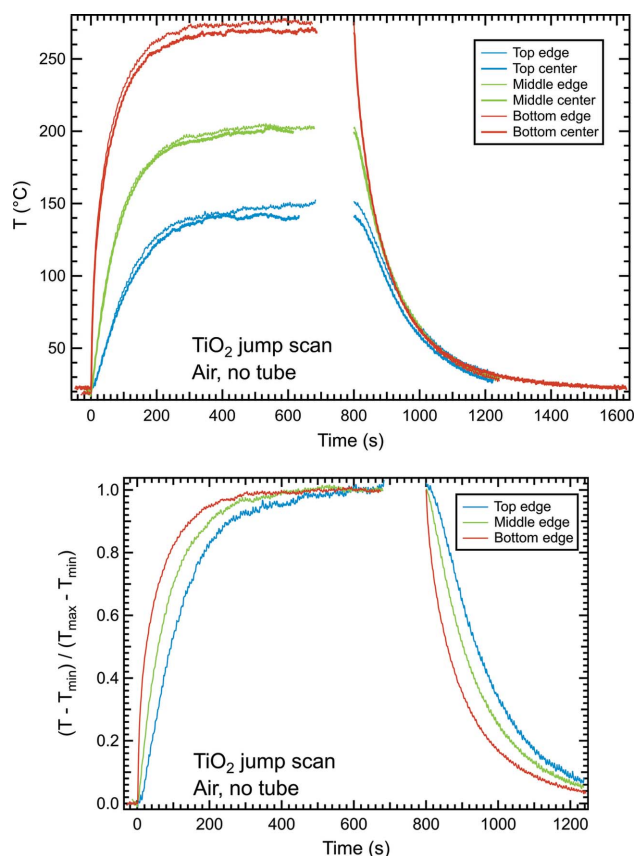

Figure 6
(Top) Power jump time series data for TiO_2. Data are plotted with offsets so that heating starts at $t = 0$ s and cooling starts at $t = 800$ s for each sample since the length of the hold was slightly different for different samples – there was no actual gap between the data collection for heating and cooling. (Bottom) Data renormalized (relative to the minimum and maximum value for each run in units of K) to allow the time scale of relaxation at different points along the rod to be compared.

Table 1
Parameters used in the TiO$_2$ model and their corresponding literature values.

Parameter	Value employed in the model	Unit	Source	Range of values in literature
Specific heat capacity†	$C_p(T)$	J (kg K)$^{-1}$	Literature	691 (at 298 K)–908 (at 700 K) (Chase, 1998)
Thermal conductivity	11.5	W (m K)$^{-1}$	Fitting	4.8–11.8 (Goodfellow, 2002)
Density	3700	kg m^{-3}	Experiment	–
Emissivity‡	0.82	–	Literature	0.82–0.92 (Kanematsu et al., 2003)
Area of heated surface	45.0504	mm^2	–	–

† The temperature-dependent heat capacity $C_p(T)$ is obtained via the following fit to TiO$_2$ heat capacity values within the range 298–700 K: $C_p(T) = -99.440 + 4.252T - 6.364 \times 10^{-3}T^2 + 3.352 \times 10^{-6}T^3 - 229.385T^{-2}$. ‡ The lower bound from the literature is selected.

$$-\mathbf{n} \cdot \mathbf{q}_{\mathrm{src}} = q_{\mathrm{src}}, \tag{1}$$

where $\mathbf{q}_{\mathrm{src}}$ is the heat flux applied at the boundary over the surface of area A and $\mathbf{n}$ is the outward unit normal vector. While in reality the light absorption processes associated with heating in an OFZ furnace have a more complex spatial dependence, this simplifying approximation is expected to be suitable for the present TiO$_2$ sample since the thermal conductivity is sufficiently high that the temperature is nearly uniform over the directly irradiated region.

The thermal transport within the bulk of the sample is described by

$$\rho \, C_p \frac{\partial T}{\partial t} - k\nabla^2 T = 0, \tag{2}$$

where ρ is the density, C_p is the specific heat capacity, T is the temperature, t is time and k is the thermal conductivity. The sample density in the present simulations was set to the experimentally measured value for the sample being studied. A temperature-dependent specific heat capacity was parameterized on the basis of literature values for TiO$_2$ measured over the range of 298–700 K (Chase, 1998) using the relationship $C_p = -99.44 + 4.252T - 6.364 \times 10^{-3}T^2 + 3.352 \times 10^{-6}T^3 - 229.385T^{-2}$ J kg^{-1} K^{-1}. The polycrystalline rod thermal conductivity was treated as a fitting parameter.

The heat loss during experiments was assumed to occur entirely between the sample surface and air with no heat transfer to the sample holder, with (a) surface-to-ambient gray-body radiation and (b) natural air convection as the main heat-transfer mechanisms between the sample and its surroundings. This assumption was found to be satisfactory for the present low-temperature experiments but inadequate for some other situations, which will be discussed in subsequent publications. The contribution from surface-to-ambient radiation at each point on the surface of the sample is given by

$$-\mathbf{n} \cdot \mathbf{q}_{\mathrm{sa}} = \epsilon \sigma (T_{\mathrm{amb}}^4 - T^4), \tag{3a}$$

where $\mathbf{q}_{\mathrm{sa}}$ is the surface-to-ambient radiative heat flux, ϵ is the surface emissivity (a constant between 0 and 1 that was set by fitting the experimental temperature profile within the constraints of previously reported values of 0.82–0.92; Kanematsu et al., 2003), σ is the Stefan–Boltzmann constant, T is the temperature at the surface of the sample and T_{amb} is the ambient temperature far from the sample (assumed to be 22°C). The contribution from natural air convection is modeled by Newton's law of cooling:

$$-\mathbf{n} \cdot \mathbf{q}_{\mathrm{air}} = h(T_{\mathrm{amb}} - T), \tag{3b}$$

where $\mathbf{q}_{\mathrm{air}}$ is the convective heat flux and h is the heat-transfer coefficient between the surface of the sample and air. In estimating h, which is a temperature- and geometry-dependent quantity, the top and bottom of the sample were assumed to be horizontal plates (Incropera et al., 2006), while the side surface was assumed to be a thin vertical cylinder (Bejan, 1993).

The governing equations described above were solved within COMSOL *Multiphysics* to simulate the temperature profiles for a polycrystalline TiO$_2$ rod experimentally measured during two sets of diffraction experiments: (1) steady-state measurements of the vertical temperature profile measured using line scans (plotted in Fig. 5), and (2) power jump measurements of the time-dependent dynamic temperature changes at six different points on the rod (plotted in Fig. 6). The model parameters that were designated as fitting parameters above were obtained by matching the simulated steady-state temperature profiles to the corresponding experimental data, and other parameters were either measured experimentally or obtained from the literature. These parameters are listed in Table 1 and were used in both steady-state simulations and time-dependent simulations.

The measured and simulated steady-state vertical temperature profiles of the TiO$_2$ sample are compared in Fig. 7. It can be seen that the agreement is generally very good between simulations and experiment. The agreement is particularly good at intermediate vertical distances of 5–25 mm from the center of the hot zone, where the differences between the model and experimental results are small relative to the scatter in the experimental data. At heights greater than 25 mm, the simulated temperature is found to be systematically lower than the experimental temperature, as would be expected if there is long-range convection in the air surrounding the sample. At shorter distances, the experimental data exhibit a temperature maximum about 1 mm above the nominal center of the hot zone, which is not predicted by the models. This discrepancy is probably due to experimental alignment issues associated with the difficulty of precisely locating the position of the lamp focus, though it could alternatively be due to the influence of experimental factors that were not included in this simple initial model (e.g. long-range convection, a more complex light absorption profile due to divergence of the lamp light or incomplete light
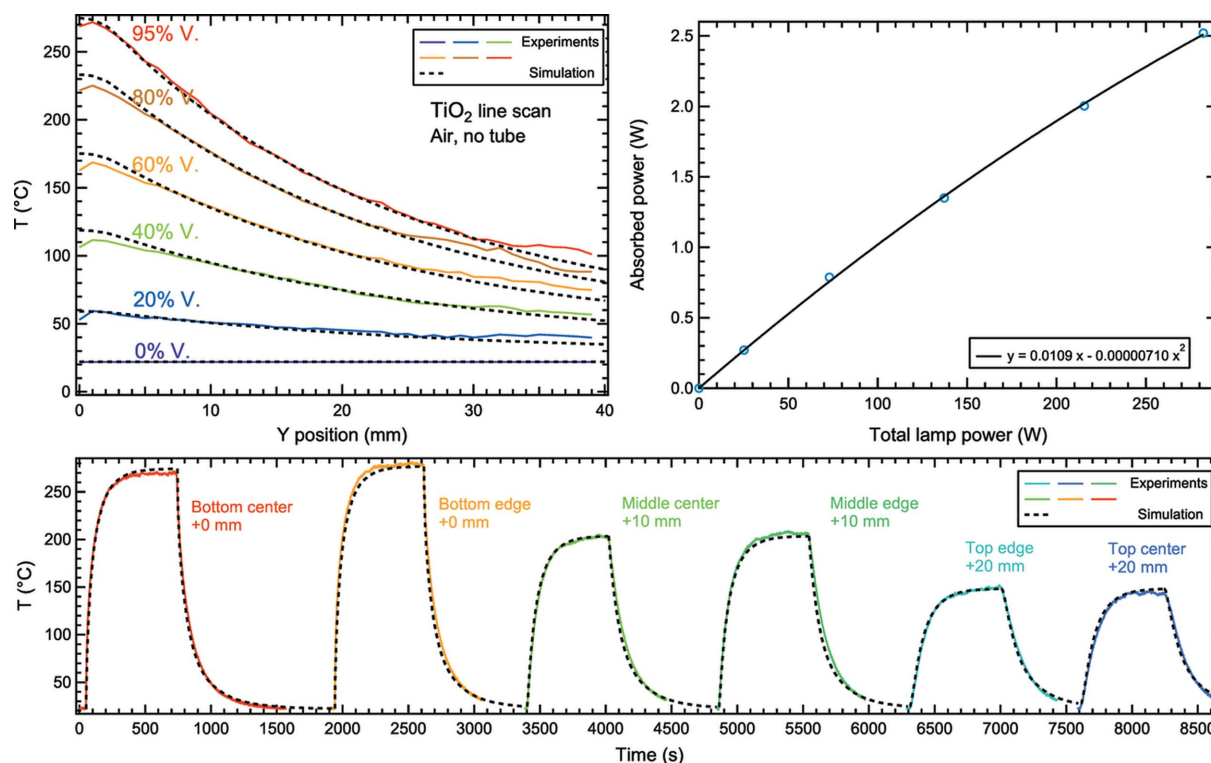
Figure 7
(Top left) Comparison of measured (solid lines) and modeled (black dashed lines) vertical line scan temperature profiles. (Top right) Plot of the power input determined via fitting the prediction to the experimental data against the experimental lamp power, along with a second-order polynomial fit to the efficiency constrained to pass through the origin. The numerical data for this plot are provided in Table S1. (Bottom) Comparison of measured and modeled temperature profiles during six power jump time series, labeled with the vertical coordinates relative to the nominal center of the focal spot from the lamps.

absorption by the sample surface, or the hemispherical shape of the sample rod end leading to additional heat loss at the tip).

While the key fitting parameters were kept constant for vertical scans carried out at different power settings, the heat flux for the sample was refined independently for each power setting. This allowed the efficiency of heating at each power level to be estimated (Fig. 7, top right, and Table S1, with further details about experimental settings provided in Table S2 and Fig. S7). The simulation results suggest that only about 1% of the electrical power applied to the lamps was absorbed by the polycrystalline TiO_2 rod. This inefficiency is believed to originate from two sources: the incomplete focusing of the radiation from the lamp on the sample rod, and the incomplete absorption of the radiation by the TiO_2 sample (which has a large band gap of about 3 eV). The simulation results suggest that the absorption efficiency of the TiO_2 sample slightly decreases as the lamp power increases. Since increasing the lamp power increases the temperature of the tungsten lamp filament and shifts the emission spectrum to higher energies, this result suggests that low-energy infrared photons (absorbed through transitions associated with atomic vibrations, intraband electronic transitions of charge carriers or impurity states) are contributing more to the sample heating than high-energy ultraviolet photons (associated with interband excitations across the sample band gap). However, it is not possible at this time to rule out the voltage depen-

dence of absorption efficiency as being a fitting artifact – further analysis of data from a wider range of samples must be carried out to assess the robustness of this result.

Very good agreement is also achieved when the same model parameters are used to simulate the power jump data (Fig. 7, bottom), indicating the robustness of the model and the parameters. Here, the data have been plotted on a common time axis for ease of visualization. The difference between the experimental and simulated temperatures is usually comparable to the scatter in the experimental data. However, it is observed that the experimentally measured sample cooling rate is generally slightly slower than the simulated cooling rate at distances far from the rod tip. This is the behavior that would be expected if there is some thermal transfer between the sample and the sample holder (which has a large thermal mass and would therefore be expected to counteract the sample cooling due to residual heat from prior heating experiments in the furnace). While these sample holder effects are not large for the TiO_2 sample, they have been found to be significantly larger for an Al_2O_3 sample. The development of more complex models is required to describe the Al_2O_3 sample, an effort that will be the subject of future work.

4. Conclusions

It is demonstrated that high-energy *in situ* diffraction measurements can be utilized to sensitively probe the

temperature profiles of large-diameter cylindrical rods – a sample geometry which is relevant to the study of crystal growth but which is not ideal for diffraction studies. This capability has been utilized to first measure and then model temperature profiles relevant to the crystal growth process carried out within an optical floating zone furnace – an inhomogeneous environment whose thermal profiles are typically unknown because of the challenges involved in accessing them. These experiments were carried out utilizing a custom synchrotron-compatible mini-FZ furnace designed for this purpose, which can be operated under a controlled gas or vacuum environment, and which is shown to be capable of melting a CuO rod (~1200°C melting point) at ~80% of its maximum lamp power. It is found that relatively simple models of thermal transport are capable of reproducing the temperature profiles experimentally measured for a poly-crystalline TiO_2 rod heated in air. Furthermore, these models can be used to determine the thermal conductivity of poly-crystalline samples having a rod geometry. This novel approach is therefore a powerful tool for parameterizing models which can be used to accurately predict temperature profiles during crystal growth and thus provide novel insights into and guidance for crystal growth. While the present furnace design does not yet enable the independent translation and rotation of two sample rods in a manner that is required for crystal growth experiments, there are ongoing efforts to develop and add these capabilities to a mini-FZ environment that can be used to carry out the type of synchrotron studies demonstrated here during actual crystal growth. Additional data collection modalities (e.g. diffraction tomography to resolve full three-dimensional temperature profiles) may become viable once these capabilities are in place.

References

Albers, P., Stark, E. & Huber, G. (1986). *J. Opt. Soc. Am. B*, **3**, 134–139.

Ashiotis, G., Deschildre, A., Nawaz, Z., Wright, J. P., Karkoulis, D., Picca, F. E. & Kieffer, J. (2015). *J. Appl. Cryst.* **48**, 510–519.

Behr, G., Löser, W., Wizent, N., Ribeiro, P., Apostu, M. O. & Souptel, D. (2010). *J. Mater. Sci.* **45**, 2223–2227.

Bejan, A. (1993). *Heat Transfer.* New York: John Wiley & Sons.

Caron, P. & Khan, T. (1999). *Aerosp. Sci. Technol.* **3**, 513–523.

Coelho, A. A. (2018). *J. Appl. Cryst.* **51**, 210–218.

Chase, M. W. (1998). *NIST-JANAF Thermochemical Tables*, 4th ed. Woodbury: The American Insitute of Physics/The American Chemical Society.

Chu, F., Thoma, D. J., McClellan, K., Peralta, P. & He, Y. (1999). *Intermetallics*, **7**, 611–620.

Damascelli, A., Hussain, Z. & Shen, Z. X. (2003). *Rev. Mod. Phys.* **75**, 473–541.

Goodfellow (2002). *Titanium Dioxide – Titania (TiO2)*, https://www.azom.com/article.aspx?ArticleID=1179, https://www.azom.com/properties.aspx?ArticleID=1179.

Hummer, D. R., Heaney, P. J. & Post, J. E. (2007). *Powder Diffr.* **22**, 352–357.

Hummer, D. R., Heaney, P. J. & Post, J. E. (2008). *Powder Diffr.* **23**, 267.

Incropera, F. P., DeWitt, D. P., Bergman, T. L. & Lavine, A. S. (2006). *Fundamentals of Heat and Mass Transfer.* Hoboken: John Wiley & Sons.

Ito, T., Yamaguchi, H., Okabe, K. & Masumi, T. (1998). *J. Mater. Sci.* **33**, 3555–3566.

Kanematsu, H., Wada, N. & Oki, T. (2003). *Plat. Surf. Finish.* **90**, 61–65.

Koohpayeh, S. M., Fort, D. & Abell, J. S. (2008). *Prog. Cryst. Growth Charact. Mater.* **54**, 121–137.

Koohpayeh, S. M., Fort, D., Bradshaw, A. & Abell, J. S. (2009). *J. Cryst. Growth*, **311**, 2513–2518.

Kosenko, A. V. & Emel'chenko, G. A. (2001). *J. Phase Equilib.* **22**, 12–19.

Majumdar, S., Sampathkumaran, E. V., Paulose, P. L., Bitterlich, H., Löser, W. & Behr, G. (2000). *Phys. Rev. B*, **62**, 14207–14211.

Mao, Z. Q., Maenoab, Y. & Fukazawa, H. (2000). *Mater. Res. Bull.* **35**, 1813–1824.

Nishimura, Y., Matsuoka, Y., Miyashita, S., Komatsu, H., Motokawa, M., Nakada, T. & Sazaki, G. (1999). *J. Cryst. Growth*, **207**, 206–213.

Pawley, G. S. (1981). *J. Appl. Cryst.* **14**, 357–361.

Prabhakaran, D. & Boothroyd, A. T. (2003). *J. Cryst. Growth*, **250**, 77–82.

Revcolevschi, A., Ammerahl, U. & Dhalenne, C. (1999). *J. Cryst. Growth*, **198–199**, 593–599.

Rodriguez, J. A., Ma, S., Liu, P., Hrbek, J., Evans, J. & Pérez, M. (2007). *Science*, **318**, 1757–1760.

Rogalski, A. & Chrzanowski, K. (2002). *Opto-Electron. Rev.* **10**, 111–136.

Seidel, J., Vaquero, J. J., Siegel, S., Gandler, W. R. & Green, M. V. (1999). *IEEE Trans. Nucl. Sci.* **46**, 485–490.

Shimura, F. (2017). *Springer Handbook of Electronic and Photonic Materials*, edited by S. Kasap & P. Capper, pp. 293–307. Cham: Springer International Publishing.

Stockert, O., Arndt, J., Schneidewind, A., Schneider, H., Jeevan, H. S., Geibel, C., Steglich, F. & Loewenhaupt, M. (2008). *Physica B*, **403**, 973–976.

Wang, H., Li, Q., Wang, C. Y., He, H., Yu, J. D. & Xu, J. Y. (2018). *Crystals*, **8**, 113.